Impact of vertical mixing parameterizations on internal gravity wave spectra in regional ocean models

Ritabrata Thakur[1], Brian K. Arbic[1], Dimitris Menemenlis[2], Kayhan Momeni[3], Yulin Pan[4], W. R. Peltier[3], Joseph Skitka[1], Matthew H. Alford[5], Yuchen Ma[3]

[1]Department of Earth and Environmental Sciences, University of Michigan, Ann Arbor, MI, USA

[2]Jet Propulsion Laboratory, California Institute of Technology, Pasadena, CA, USA

[3]Department of Physics, University of Toronto, Toronto, Canada

[4]Department of Naval Architecture and Marine Engineering, University of Michigan, Ann Arbor, MI, USA

[5]Scripps Institution of Oceanography, University of California San Diego, La Jolla, CA, USA

Key Points:

- Regional ocean simulations are ideal for examining sensitivity of IGW spectra to model mixing parameters
- Turning off the KPP background yields more realistic IGW vertical structure in high-resolution regional models
- IGW spectra are most correctly estimated in models away from tidal generation sites and lateral boundaries

Corresponding author: Ritabrata Thakur, `ritabrata90official@gmail.com`

Abstract

We present improvements in the vertical wavenumber spectrum of the internal gravity wave continuum in high-resolution regional ocean simulations. We focus on model sensitivities to mixing parameters and comparisons to McLane moored profiler observations in a Pacific region near the Hawaiian Ridge, which features strong semidiurnal tidal beams. In these simulations, the modeled continuum exhibits high sensitivity to the background mixing components of the K-Profile Parameterization (KPP) vertical mixing scheme. Without the KPP background mixing, stronger vertical gradients in velocity are sustained in the simulations and the modeled kinetic energy and shear spectral slopes are significantly closer to the observations. The improved representation of internal wave dynamics in these simulations makes them suitable for improving ocean mixing estimates and for the interpretation of satellite missions such as the Surface Water and Ocean Topography (SWOT) mission.

Keywords: internal gravity waves, vertical wavenumber spectra, MITgcm, KPP mixing parameterization

Plain Language Summary

Internal waves exist in the ocean interior due to differences in fluid densities. Breaking internal waves cause mixing, which has important effects on ocean temperatures and nutrients. Interactions between internal tides generated by tidal flow over bathymetric features and near-inertial waves generated by wind yield a spectrum of internal waves at many frequencies. Here, we compare the internal wave spectrum in high-resolution numerical simulations of a region in the North Pacific with observations from moored instruments. We study the effects of the "background" mixing components of the widely used K-profile parameterization (KPP) vertical mixing scheme on the vertical structure of the internal wave field. The KPP background parameterizes the mixing action of internal waves, which is not resolved in coarser-resolution global ocean models. In our high-resolution simulations, the internal wave field is highly active, and the KPP background components turn out to be mostly redundant in this setting. Indeed, the modeled internal wave field lies closer to observations when we turn off the KPP background. Improved internal wave representation in ocean models can play an important role in the accurate representation of internal-wave-driven mixing in ocean simulations and interpretation of internal wave signatures from the upcoming SWOT mission.

1 Introduction

This paper focuses on the vertical structure of the internal gravity wave (IGW; also simply "internal wave", or IW) spectrum in regional ocean models. We examine model sensitivities to vertical grid spacing and vertical mixing parameterizations.

At tidal frequencies, IWs are called internal tides (ITs) and are primarily generated by large-scale barotropic tides moving over topography (e.g., Baines, 1982; Bell, 1975). High-frequency changes in wind forcing generate near-inertial (NI) IWs at the ocean surface, having frequencies close to the Coriolis frequency. The high-frequency IW continuum, also known as the Garrett-Munk spectrum (Garrett & Munk, 1972, 1975; Cairns & Williams, 1976), is thought to arise from nonlinear interactions of ITs, NI motions and the IW continuum. The variable distribution of IWs and IW-generated turbulence (Kunze, 2017b) inspire continued interest due to its importance in vertical temperature redistribution (e.g., as in the Arctic; D'Asaro & Morison, 1992) and the global overturning circulation (Kunze, 2017a), their role in the enhancement of primary productivity by redistribution of nutrients (X. Pan et al., 2012), and important feedback to climate (MacKinnon et al., 2017; Whalen et al., 2020).

Global high-resolution ocean general circulation models with simultaneous tidal and atmospheric forcing carry a partially-resolved IW continuum (Müller et al., 2015; Rocha, Chereskin, et al., 2016; Arbic et al., 2018). These global models fall short of representing the real ocean due to a lack of resolution and/or insufficient parameterization of unresolved sub-grid scale physical processes such as IW breaking. Regional ocean models have been shown to display improved IW spectra over those in the global models when run at higher horizontal and vertical resolutions, as long as the lateral boundary forcing includes remotely-generated IWs from a global IW model (Mazloff et al., 2020; Nelson et al., 2020). Such remotely-forced regional models run over short periods are relatively affordable computationally and can be used to study the sensitivity of the IW continuum due to changes in model parameters.

Here, we study high-resolution regional simulations of the Massachusetts Institute of Technology general circulation model (MITgcm; Marshall et al., 1997) forced at their lateral boundaries by a global MITgcm simulation, named LLC4320, that has been widely studied (e.g., Rocha, Chereskin, et al., 2016; Rocha, Gille, et al., 2016; Savage et al., 2017; Su et al., 2018). Regional simulations forced by LLC4320 have recently been used to study the sensitivity of the IW continuum to model resolution (Nelson et al., 2020) and to under-
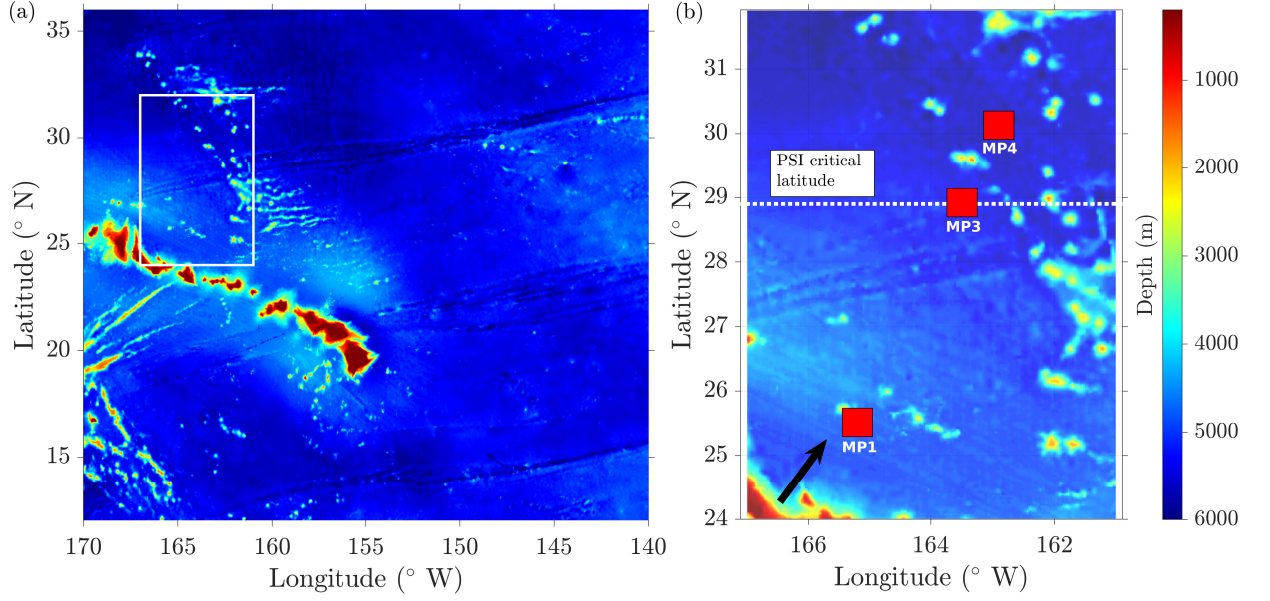
stand the mechanisms involved in the formation of the continuum (Y. Pan et al., 2020). In this paper, we study the sensitivity of the IW vertical wavenumber spectra to the cumulative effect of the background vertical viscosity and diffusivity components of the K-profile parameterization (KPP; Large et al., 1994).

In our regional simulations, we focus on a region in the Pacific Ocean northward of Hawaii (Fig 1). This region has heightened semi-diurnal (M_2) ITs that propagate northward from the islands (Fig 1 (b)) and undergo parametric subharmonic instability (PSI) at the critical latitude of 28.8° N, where the local inertial frequency is half of the M_2 tidal frequency. In contrast with the shear field at other latitudes in this region, marginally-stable shear layers with elevated NI energy generated via PSI of the IT are observed at 28.8° N (Alford et al., 2007). The northward-propagating ITs also interact with southbound IT beams from the Aleutian Ridge (not in the simulation domain), generating a complex IT field (e.g., Zhao et al. (2010); Alford et al. (2019)). We present improvements in the modeled IW vertical structure in these regional simulations by comparing them to observational data obtained using McLane moored profilers (Doherty et al., 1999; Morrison et al., 2001) (Fig 1 (b)). We find that the vertical wavenumber spectra of KE and shear shows appreciable improvement when the KPP background mixing is turned off. We also discuss the characteristics of shear spectra across different frequency bands in simulations with the KPP background turned off. The model captures the vertical structure of the NI band, which is an important component of the total shear, whereas the primary deficiency of the model relative to observations lies in the high-frequency (supertidal) IW continuum. We further study the sensitivity of modeled strain spectra to the KPP background components and quantify spectral improvements with model vertical resolution.

2 Data and methods

2.1 MITgcm model

Using MITgcm, we simulate a $6° \times 8°$ region north of the French Frigate Shoals, Hawaii, in the Pacific Ocean as shown in Fig 1. We study a suite of regional simulations with 109, 153, and 264 z-levels in the ocean and a constant horizontal grid spacing of $1/48°$ (~2km near the equator). These regional simulations begin on 1 March 2012 and run for 73 days with initial fields taken from the global LLC4320 simulation, which employs the same grid spacing in the horizontal and 90 z-levels in the vertical direction (Rocha, Chereskin, et al.,

Figure 1. (a) The domain of study north of Hawaii is marked by the white rectangle. (b) An expanded view of the simulation domain. The locations of the McLane moored profilers (MP1, MP3, and MP4) are marked as red solid blocks. The white dashed line at 28.8° N is the critical latitude for parametric subharmonic instability (PSI; e.g., MacKinnon et al., 2013). The solid black arrow shows the primary direction of the energy flux of an M_2 tidal beam (as marked from a numerical model in Fig 1 of Alford et al. (2007)). The model bathymetry from Smith and Sandwell (1997) is shown in color in each subplot.

2016; Savage et al., 2017). The vertical level thicknesses of our new high-resolution regional simulations are equal to those in LLC4320 up to a certain depth depending on the model resolution and stay constant below that to the bottom of the ocean (Fig S1). At the lateral boundaries, the regional simulations are forced by fields of LLC4320 which also includes remotely-generated IWs. All the simulations are forced with realistic atmospheric fields and the astronomical tidal potential. Velocities, temperature, and salinity are stored at hourly time steps. (More in the SI.)

2.2 Observations

McLane moored profilers (MP) are deployed on oceanographic moorings and vertically profile the water column at 10–33 cm s^{-1} (Doherty et al., 1999). MPs record velocities, temperature, conductivity, pressure, and other oceanic variables in hourly intervals. We use data from three MPs, deployed in the Pacific during the Internal Waves Across the Pacific experiment (Alford et al., 2007) along track 249 of TOPEX-Poseidon. The MP locations are marked as MP1 (194.8° E, 25.5° N), MP3 (196.5° E, 28.8° N), and MP4 (197.1° E, 30.1° N) in Fig 1 (b). The MP data are available in the depth range of 85–1384m with a vertical resolution of ∼2m, from 25 April–05 June 2006 at MP1 and MP3, and from 25 April–17 May 2006 at MP4.

2.3 Spectra calculations

Prior to vertical wavenumber spectra calculations with both model output and MP data, the horizontal velocities and the depths are WKBJ-scaled using local buoyancy frequency following Leaman and Sanford (1975) and interpolated to equally-spaced vertical coordinates (see Fig S2 and text in the SI). All vertical wavenumber spectra presented in this paper are averages of individual spectra over the model runtime and MP deployment periods, giving ∼1700 degrees of freedom (dof) for models and 530–950 dof for MPs assuming the spectra to be mutually independent. Velocities at the top and bottom of the depth range of spectra calculation are smoothly tapered to zero values using a Hanning window, and the lost variance due to this tapering is added back to the total variance. There is no segmenting of data in the vertical direction in our computations of spectra. (More in the SI.)

3 Model parameterizations

The interior vertical mixing parameterization scheme in the simulations is KPP (Large et al., 1994), and the horizontal mixing is governed by the Leith parameterization for 2D turbulence (Leith, 1968). The Leith scheme is modified with an added damping to the divergent flow field (Fox-Kemper & Menemenlis, 2008) specifically developed for the stability of global ocean models. The effect of the Leith scheme on the modeled IW fields in high-resolution regional models is not considered here but will be discussed in future studies.
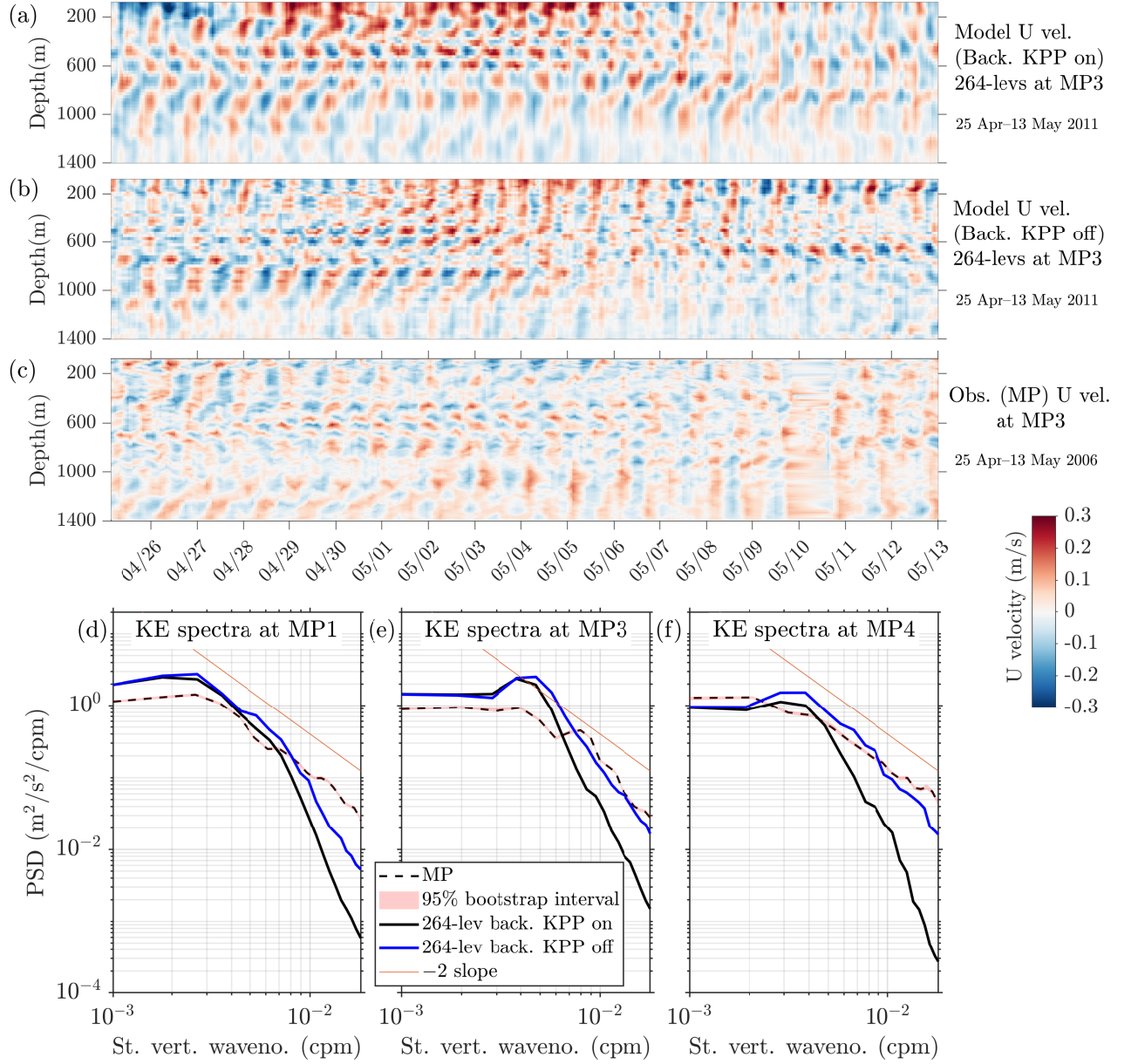
There are three controlling parameters which cumulatively act within the KPP scheme for the ocean interior mixing away from the upper mixed layer: (a) Richardson number-dependent shear-driven mixing, (b) a constant background mixing to compensate for the breaking of unresolved IWs, set to $\mathcal{O}(10^{-4})$ m²s⁻¹ as viscosity in the momentum equations and $\mathcal{O}(10^{-7})$ m²s⁻¹ for temperature and salt diffusivity in LLC4320, and (c) double-diffusive mixing (not implemented in any of the simulations here). The KPP background has constant damping coefficients for energy dissipation that act at all spatial locations, time steps, and vertical scales of the simulations. Also, if the fluid column becomes convectively unstable, it undergoes immediate mixing in the simulations.

With an increase in vertical resolution, models better capture the small-scale density and velocity fluctuations associated with an improved IW field. This raises the question of whether the KPP background, which parameterizes IW-driven mixing in coarser-resolution models that have reduced IW activity, would still be needed with an increase in model resolution. In the following sections, we quantify the effect of KPP background on the modeled spectra primarily using results from the highest-resolution (264-level) simulations (with results from lower-resolution simulations summarized in the SI).

4 Spectral estimates and discussion

In the high-wavenumber regime, Cairns and Williams (1976)'s revision of the Garrett and Munk (1972, 1975) spectrum—GM76—predicts a universal form of the kinetic energy (KE) spectrum $E(m) \sim m^{-2}$, where m are the (stretched) vertical wavenumbers defined here as the inverse of the stretched depths (also see the SI). The GM76 shear and strain spectra derived from $E(m)$ have spectral slopes of m^0 at high-wavenumbers. However, extensive high-resolution observations have demonstrated that these spectral slopes are variable in the ocean (as reviewed in Polzin and Lvov (2011)). Therefore, in the following discussions,

Figure 2. Time-depth plots of zonal (U) velocity from 264-level simulations at the MP3 location and over the depth range of 80–1400 m, with the KPP background (a) on and (b) off, are compared to observed zonal velocity in (c). The model output and the observations are from the same days of the year but different years. In (d–f), KE spectra in the same depth range for 264-level simulations (solid curves) at locations marked in Fig 1 (b) are compared to observed KE spectra (dashed curves) in the depth range of 85–1384m. The solid black curves are the modeled KE spectra with the KPP background on, while the blue curves are the modeled KE spectra with the KPP background components set to zero. 95% bootstrap confidence intervals on the means of the observed KE spectra are drawn in each as light red shading (for simulations, the 95% confidence intervals are smaller than the thickness of the curves). The GM76 spectral slope of −2 is drawn in each for reference. KE spectra are also shown in Figs S3, S4, and S5 in the SI.

170 we will consider the observed spectra as the "truth" in our comparison of the modeled and

171 observed spectra and include GM76 spectral slopes as reference.

4.1 Kinetic energy spectra

173 In our regional domain (Fig 1 (b)), vertical wavenumber spectra of KE from the ob-

174 servations differ from the GM76 slope of m^{-2} (Fig 2). At wavenumbers higher than 0.02

175 cpm (not shown), observed KE spectral slopes from the MPs are nearer to -2.4. Combined

176 with the frequency spectral slopes at these sites, this value is closer to the induced-diffusion-

177 dominated solutions predicted by wave turbulence theory (e.g., Lvov et al., 2010; Y. Pan et

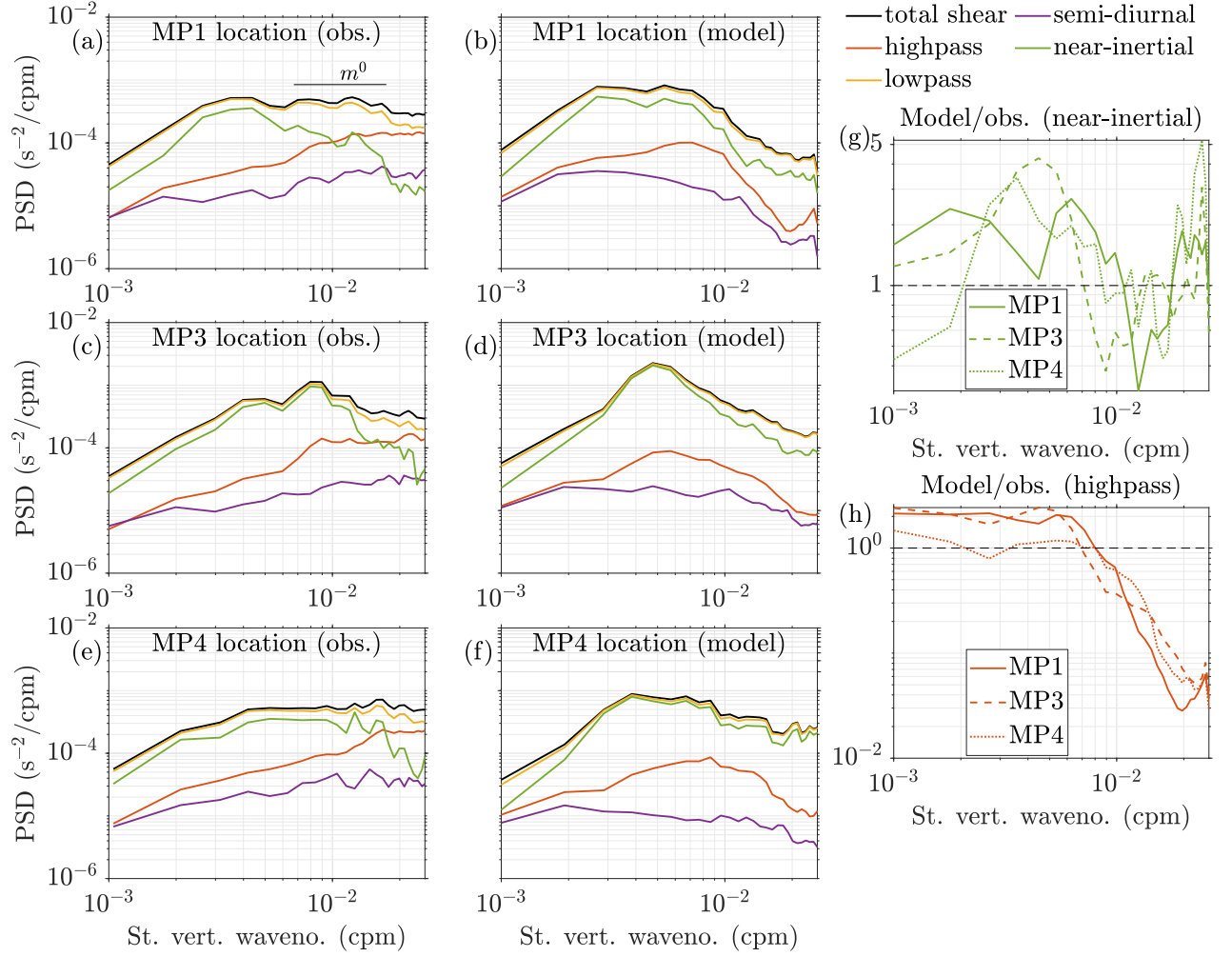178 al., 2020) than to the GM76 slope.

179 We find that the modeled velocities and the KE spectra are sensitive to the KPP back-

180 ground (Fig 2). A comparison of zonal velocities from the 264-level simulations (Fig 2 (a,b))

181 with that from the observations (Fig 2 (c)) shows that the velocity field has more small-scale

182 features when the KPP background diffusivity and viscosity are both set to zero (Fig 2 (b)).

183 Although a perfect agreement between the velocity field from the simulations and the ob-

184 servations is not expected, energetic events, including those due to tidally-induced periodic

185 flows, have sharper vertical gradients in the simulation without the KPP background (Fig

186 2 (b)) roughly similar to that seen in the observations (Fig 2 (c)), whereas these gradients

187 are more diffused in the simulation where the KPP background is kept on and has the same

188 values as that of the KPP background in global LLC4320 (Fig 2 (a)).

189 The effect of turning the KPP background off on the IW field is seen in the comparison

190 of the spectral slopes of the modeled KE spectra to that of the observed KE spectra (Fig

191 2 (d–f)). At low wavenumbers (<0.003 cpm), both observed and modeled KE spectra with

192 and without KPP background roll off to a limiting slope value near zero. The observed

193 and the modeled spectra disagree within a factor of two at wavenumbers <0.003 cpm at all

194 three MP locations. This disagreement may be due to the differences in the overall oceanic

195 eddy, tidal or near-inertial fields given that the observations and the model simulations are

196 not contemporaneous. The modeled KE spectra with and without the KPP background

197 begin diverging at wavenumbers higher than 0.004 cpm suggesting a vertical scale where

198 the KPP background starts to become active in the simulations. This vertical scale has a

199 small variability depending on the geographical location within the domain and the vertical

200 resolution of the model (Fig S3) and is also different in different frequency bands (Fig S4).

However, the general conclusion is that the high-wavenumber spectral slopes of the modeled KE spectra with the KPP background turned off lie significantly closer to the observed KE spectra from the MPs (Figs 2 (d–f) and S3).

The greatest improvement in the modeled KE spectra without the KPP background is seen at the MP4 location which is farthest from the generation site of the M_2 tidal beam. The variance at the highest wavenumber is $\sim$40 times higher at MP4 with the KPP background turned off (Fig 2 (f)). The magnitude of increase in spectral variance at MP1 and MP3 at the highest wavenumber without the KPP background are comparable to each other but less than that at MP4. At MP3, which is $\sim$500km from the M_2 IT generation site, the improved modeled IW continuum spectral levels are an order of magnitude higher when the KPP background is turned off (Fig 2 (e)), and the levels display a good agreement with the observed KE spectrum. However, the improved modeled spectrum at MP1 is still relatively deficient in the IW continuum. As all the locations have similar vertical stratification, this difference in the spectral improvement and the disagreement between the modeled and the observed spectra could most likely be due to the degree of proximity to the IT generation site. With MP1 being nearer to the IT generation site (Fig 1 (b)), the nonlinear interactions giving rise to the IW continuum have insufficient time to develop, when compared to MP3 or MP4, giving rise to a weaker overall KE spectrum.

Spectral improvement with the KPP background turned off is also observed in the 109- and 153-level simulations (Fig S3) signifying that in both high (264-level) and moderate vertical resolution simulations (109- and 153-levels), the KPP background may have to be turned off to achieve a realistic IW continuum in regional models. We also note that turning off the KPP background improves the modeled IW continuum at all frequencies as the high-wavenumber spectral variances are higher in both the highpass (high-frequency or supertidal) and lowpass frequency bands around a cutoff of 11.5 hr as well as in the semidiurnal and near-inertial frequency bands (shown for 264-level in Fig S4). The lowpass band includes semidiurnal and diurnal tides, and near-inertial and subtidal flows, while the highpass band includes the supertidal IW continuum. We further observe that the high-wavenumber KE variance in the deeper ocean (1500–4000m) progressively increases with an increase in the model vertical resolution (Fig S5).

Figure 3. Shear spectra $\Phi(m)$ in different frequency bands from MP observations in (a), (c), and (e) are compared to modeled shear spectra from the 264-level simulation with the KPP background turned off in (b), (d), and (f). In each subplot, black is total shear, red is highpass or supertidal shear (>11.5 hr), yellow is lowpass shear (<11.5 hr), purple is semi-diurnal shear (11.5–13.5 hr), and green is NI shear (90–110% of the local inertial period). The high-wavenumber m^0 slope of the GM76 shear spectrum is denoted in (a). (g–h) The ratio of the modeled shear to observed shear, for the NI and highpass bands, respectively.

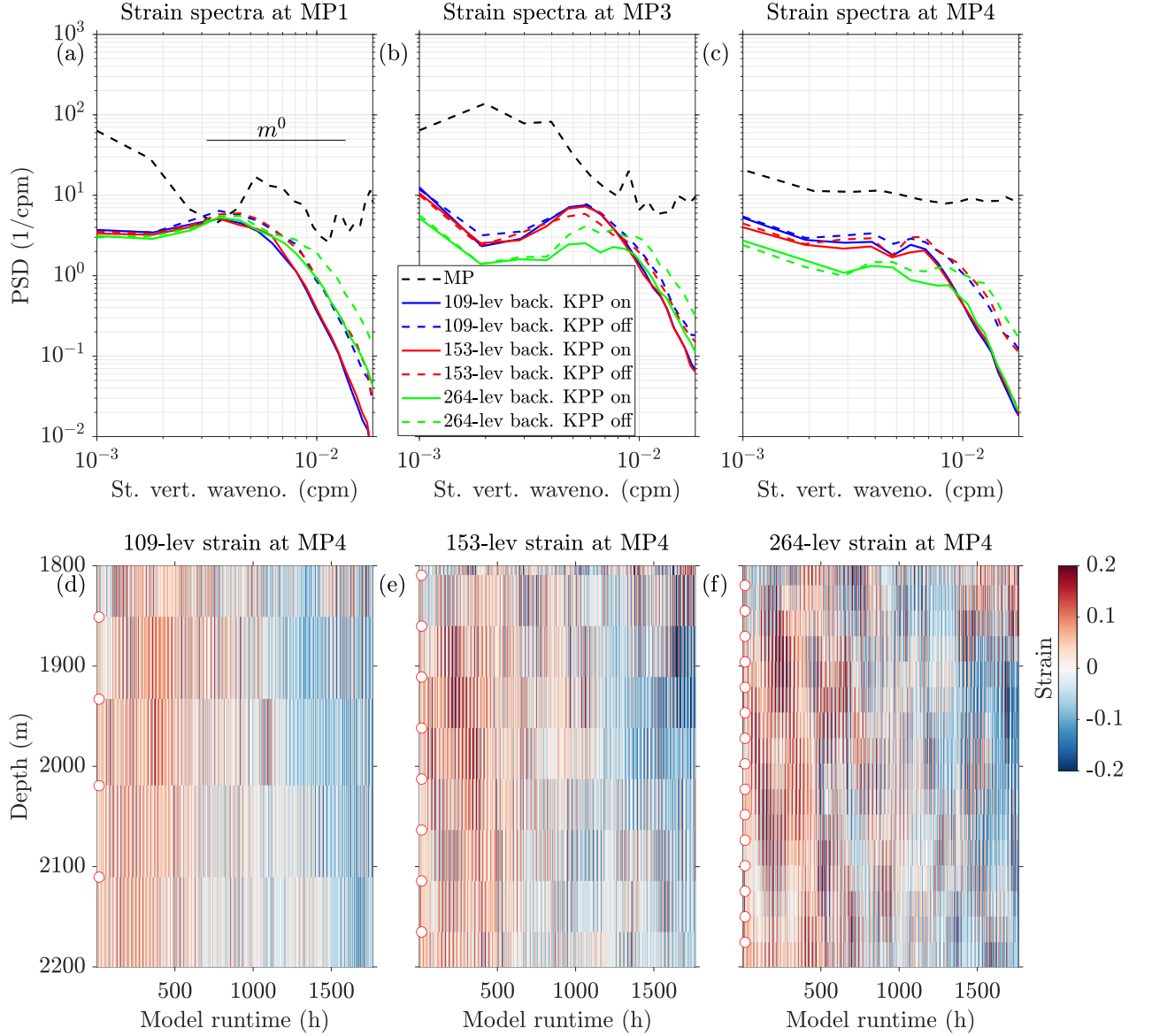### 4.2 Shear and strain spectra

The vertical shear spectrum is defined as $\Phi(m) = (2\pi m)^2 E(m)$ (Gregg et al., 1993). In what follows, we first describe the shear characteristics of the regional domain using MP observations and then compare it to the shear spectra from the 264-level simulation with the KPP background turned off to understand the strengths and deficiencies of the modeled shear in different frequency bands.

The observed shear from MPs is dominated by slowly-varying (lowpass) flows with periods greater than 11.5 hr at all vertical scales (Fig 3 (a, c, e)). As expected, the NI band contributes significantly to the total shear. Alford et al. (2017) find that the shear layers at the PSI latitude (MP3) persist for $\mathcal{O}(25)$ days. In contrast, the shear layers persist for $\mathcal{O}(7)$ days at other MP locations. This is reflected in the NI shear spectrum at MP3 which has the highest variance among the three locations (Fig 3 (c) compared to (a, e)). The NI shear spectra have positive slopes up to 0.003 cpm at MP1 and $\sim$0.01 cpm at MP3 and MP4, after which they lose variances by an order of magnitude at MP1 and MP3. However, the NI shear at MP4 does not have much vertical variability and also has lower peak shear variance. The NI shear is geographically variable at small vertical scales in that it is a factor of 2–5 lower than the total shear at the highest wavenumber at MP3 and MP4 but approximately 20 times lower at MP1. The highpass shear is lower than the NI shear at low wavenumbers but has a higher variance than the NI shear above 0.01 cpm.

Similar to the observations, the modeled 264-level shear with the KPP background turned off is dominated by slowly-varying flows (Fig 3 (b, d, f)). The integrated modeled shear at the PSI latitude (MP3; Fig 3 (d)) is 1.2–2.5 times higher than at MP1 and MP4 (Fig 3 (b, f)) and attains the highest peak shear among the three locations. Considering the ratio of variance in the NI band (Fig 3 (g)), the modeled and the observed shear show reasonable agreement. In the highpass band, the model does not capture the transition as seen in the observed shear at 0.01 cpm as the modeled highpass shear remains lower than the respective modeled NI shear at all wavenumbers (e.g., comparing Fig 3 (a) and (b)). The ratio of the modeled to observed highpass shear (Fig 3 (h)) shows that in contrast to the other two locations, the modeled highpass shear at MP4 is within a factor of 1.5 of the observed highpass shear for a decade of wavenumbers from 10^{-3}–10^{-2} cpm. However, unlike the NI shear ratio, the modeled to observed highpass shear ratio decreases after 0.007–0.008 cpm and the modeled highpass shear is more than an order of magnitude less than the

observations at the highest wavenumber (Fig 3 (h)). This reduction in high-wavenumber highpass shear variance could be attributed to the inability of the model to represent the cascade of energy to these vertical scales from low-frequency and NI motions due to a model grid spacing that is too coarse or excessive damping by improper model parameterizations.

The modeled spectra of strain $(N^2 - \overline{N^2})/\overline{N^2}$, with N being the Brunt–Väisälä frequency and overbar denoting time mean, are lower in variance relative to the observed strain spectra (Fig 4 (a–c)). Except in the small range of 0.003–0.004 cpm at the MP1 location (Fig 4 (a)), the model is always lower than the observations in strain variance even in the highest resolution (264-level) simulations. Turning off the KPP background increases the strain variance by less than an order of magnitude at high wavenumbers, but this increase is not sufficient enough to bring the modeled strain variance up to the level of the observations. The largest increase in variance by turning off the KPP background is seen at MP4 (Fig 4 (c)), the location farthest from the IT generation site (Fig 1 (b)). Except in the NI band and over a small range of wavenumbers, the modeled strain variance is an order of magnitude too low over the majority of the wavenumbers in all frequency bands (Fig S6). In the deeper ocean, an appreciable increase in the representation of modeled small-scale strain is observed when the vertical resolution of the model is progressively increased (Fig 4 (d–f)). This improvement with an increase in the model vertical resolution is reflected in the deep-ocean (1500–4000m) strain spectra (Fig S7) which have the highest variance in the 264-level simulations. Improving the modeled strain may involve refined temporal and spatial resolution as well as understanding the effect of other model parameterizations.

Figure 4. (a–c) Observed strain spectra (black dashed curves) for different locations in the depth range of 85–1384m are compared to modeled strain spectra from 109-, 153-, and 264-level simulations in the depth range of 80–1400m with and without the KPP background components. (d–f) The deeper ocean modeled strain at MP4 location without the KPP background components for three different vertical resolutions of the model. The filled circles on the y-axis are the locations of the model z-levels. The ratios of the modeled to observed strain in different frequency bands are in Fig S6 and the modeled strain spectra in the deep ocean (1500–4000m) are in Fig S7.

5 Conclusions

Regional simulations with higher vertical and horizontal resolutions can display improved IW spectra over those in the global simulations, as long as they are forced at their lateral boundaries by remotely-generated IWs from global simulations (Mazloff et al., 2020; Nelson et al., 2020). High vertical resolution regional simulations at the same horizontal grid spacing ($\sim$2km) as the global LLC4320 are studied in this paper to explore the sensitivities of the modeled IW vertical structure to model parameterizations, in particular, the background mixing components of the K-profile parameterization (KPP; Large et al. (1994)). We show that the kinetic energy variance at the high vertical-wavenumber IW continuum increases and lies closer to the observations when the KPP background components are set to zero, with the agreement most notable in locations away from the tidal generation site of the Hawaiian islands. Thus, when high-resolution ocean models start resolving IWs, the KPP background, which compensates for breaking IWs in coarse-grid models that do not represent IW processes at all, should be turned down or even off to maintain the proper spectral level of the IW continuum.

The higher shear at the parametric subharmonic instability critical latitude is captured in the simulations with the KPP background turned off. The ability of the model to represent near-inertial shear, a critical component of the total IW shear, at all vertical wavenumbers is an encouraging start in understanding the space-time variability of IW shear using ocean models. However, the high-frequency or supertidal ($>$11.5 hr) component of the IW continuum shear is not adequately captured in this model. The simulations with the KPP background turned off are weaker in strain variance relative to observed strain. The increase in modeled strain variance with the KPP background turned off is not enough to elevate the modeled spectral levels to that of the observations. This work can be developed in a few directions to address these model deficiencies and further improve the modeled IW continuum. We have not studied the sensitivity of the modeled spectra to the frequency of atmospheric forcing updates. We have also not explored the effects of increasing the horizontal resolution and the role of other model mixing parameterizations, most importantly, the Richardson number-dependent shear-driven mixing component of the KPP and the Leith damping. These issues are likely to be important for accurate modeling of high-frequency shear and strain and will be discussed in future papers.

Acknowledgments

6 Open Research

The McLane moored profiler observations, regional MITgcm model simulation output, and the analysis codes used in this study are hosted at Harvard Dataverse at `https://doi.org/10.7910/DVN/HOVAPO`. The global LLC4320 output is available at `https://data.nas.nasa.gov/ecco/`.

References

Alford, M. H., MacKinnon, J., Zhao, Z., Pinkel, R., Klymak, J., & Peacock, T. (2007). Internal waves across the Pacific. *Geophysical Research Letters*, *34*(24).

Alford, M. H., MacKinnon, J. A., Pinkel, R., & Klymak, J. M. (2017). Space–time scales of shear in the North Pacific. *Journal of Physical Oceanography*, *47*(10), 2455–2478.

Alford, M. H., Simmons, H. L., Marques, O. B., & Girton, J. B. (2019). Internal tide attenuation in the North Pacific. *Geophysical Research Letters*, *46*(14), 8205–8213.

Arbic, B. K., Alford, M. H., Ansong, J. K., Buijsman, M. C., Ciotti, R. B., Farrar, J. T., . . . others (2018). A primer on global internal tide and internal gravity wave continuum modeling in HYCOM and MITgcm. *New Frontiers in Operational Oceanography*, 307–392.

Baines, P. G. (1982). On internal tide generation models. *Deep Sea Research Part A. Oceanographic Research Papers*, *29*(3), 307–338.

Bell, T. (1975). Topographically generated internal waves in the open ocean. *Journal of Geophysical Research*, *80*(3), 320–327.

Cairns, J. L., & Williams, G. O. (1976). Internal wave observations from a midwater float,

346   2. *Journal of Geophysical Research*, *81*(12), 1943–1950.

347 D'Asaro, E. A., & Morison, J. H. (1992). Internal waves and mixing in the Arctic Ocean.
348   *Deep Sea Research Part A. Oceanographic Research Papers*, *39*(2), S459–S484.

349 Doherty, K., Frye, D., Liberatore, S., & Toole, J. (1999). A moored profiling instrument.
350   *Journal of Atmospheric and Oceanic Technology*, *16*(11), 1816–1829.

351 Fox-Kemper, B., & Menemenlis, D. (2008). Can large eddy simulation techniques im-
352   prove mesoscale rich ocean models? *Washington DC American Geophysical Union*
353   *Geophysical Monograph Series*, *177*, 319–337.

354 Garrett, C., & Munk, W. (1972). Space-time scales of internal waves. *Geophysical Fluid*
355   *Dynamics*, *3*(3), 225–264.

356 Garrett, C., & Munk, W. (1975). Space-time scales of internal waves: A progress report.
357   *Journal of Geophysical Research*, *80*(3), 291–297.

358 Gregg, M., Winkel, D., & Sanford, T. (1993). Varieties of fully resolved spectra of vertical
359   shear. *Journal of physical oceanography*, *23*(1), 124–141.

360 Kunze, E. (2017a). The internal-wave-driven meridional overturning circulation. *Journal*
361   *of Physical Oceanography*, *47*(11), 2673–2689.

362 Kunze, E. (2017b). Internal-wave-driven mixing: Global geography and budgets. *Journal*
363   *of Physical Oceanography*, *47*(6), 1325–1345.

364 Large, W. G., McWilliams, J. C., & Doney, S. C. (1994). Oceanic vertical mixing: A review
365   and a model with a nonlocal boundary layer parameterization. *Reviews of Geophysics*,
366   *32*(4), 363–403.

367 Leaman, K. D., & Sanford, T. B. (1975). Vertical energy propagation of inertial waves: A
368   vector spectral analysis of velocity profiles. *Journal of Geophysical Research*, *80*(15),
369   1975–1978.

370 Leith, C. E. (1968). Diffusion approximation for two-dimensional turbulence. *The Physics*
371   *of Fluids*, *11*(3), 671–672.

372 Lvov, Y. V., Polzin, K. L., Tabak, E. G., & Yokoyama, N. (2010). Oceanic internal-wave
373   field: Theory of scale-invariant spectra. *Journal of physical oceanography*, *40*(12),
374   2605–2623.

375 MacKinnon, J. A., Alford, M. H., Sun, O., Pinkel, R., Zhao, Z., & Klymak, J. (2013).
376   Parametric subharmonic instability of the internal tide at 29 N. *Journal of Physical*
377   *Oceanography*, *43*(1), 17–28.

378 MacKinnon, J. A., Zhao, Z., Whalen, C. B., Waterhouse, A. F., Trossman, D. S., Sun,

O. M., ... others (2017). Climate process team on internal wave–driven ocean mixing. *Bulletin of the American Meteorological Society*, *98*(11), 2429–2454.

Marshall, J., Adcroft, A., Hill, C., Perelman, L., & Heisey, C. (1997). A finite-volume, incompressible Navier Stokes model for studies of the ocean on parallel computers. *Journal of Geophysical Research: Oceans*, *102*(C3), 5753–5766.

Mazloff, M. R., Cornuelle, B., Gille, S. T., & Wang, J. (2020). The importance of remote forcing for regional modeling of internal waves. *Journal of Geophysical Research: Oceans*, *125*(2), e2019JC015623.

Morrison, A., Toole, J., Lukas, R., Worrilow, S., & Doherty, K. (2001). Results from the first successful field deployment of the McLane moored profiler. In *MTS/IEEE Oceans 2001. An Ocean Odyssey. Conference Proceedings (IEEE Cat. No. 01CH37295)* (Vol. 2, pp. 949–955).

Müller, M., Arbic, B. K., Richman, J. G., Shriver, J. F., Kunze, E. L., Scott, R. B., ... Zamudio, L. (2015). Toward an internal gravity wave spectrum in global ocean models. *Geophysical Research Letters*, *42*(9), 3474–3481.

Nelson, A., Arbic, B., Menemenlis, D., Peltier, W., Alford, M., Grisouard, N., & Klymak, J. (2020). Improved internal wave spectral continuum in a regional ocean model. *Journal of Geophysical Research: Oceans*, *125*(5), e2019JC015974.

Pan, X., Wong, G. T., Shiah, F.-K., & Ho, T.-Y. (2012). Enhancement of biological productivity by internal waves: observations in the summertime in the northern South China Sea. *Journal of Oceanography*, *68*(3), 427–437.

Pan, Y., Arbic, B. K., Nelson, A. D., Menemenlis, D., Peltier, W., Xu, W., & Li, Y. (2020). Numerical investigation of mechanisms underlying oceanic internal gravity wave power-law spectra. *Journal of Physical Oceanography*, *50*(9), 2713–2733.

Polzin, K. L., & Lvov, Y. V. (2011). Toward regional characterizations of the oceanic internal wavefield. *Reviews of Geophysics*, *49*(4).

Rocha, C. B., Chereskin, T. K., Gille, S. T., & Menemenlis, D. (2016). Mesoscale to sub-mesoscale wavenumber spectra in Drake Passage. *Journal of Physical Oceanography*, *46*(2), 601–620.

Rocha, C. B., Gille, S. T., Chereskin, T. K., & Menemenlis, D. (2016). Seasonality of submesoscale dynamics in the Kuroshio Extension. *Geophysical Research Letters*, *43*(21), 11–304.

Savage, A. C., Arbic, B. K., Alford, M. H., Ansong, J. K., Farrar, J. T., Menemenlis, D.,

... others (2017). Spectral decomposition of internal gravity wave sea surface height in global models. *Journal of Geophysical Research: Oceans*, *122*(10), 7803–7821.

Smith, W. H., & Sandwell, D. T. (1997). Global sea floor topography from satellite altimetry and ship depth soundings. *Science*, *277*(5334), 1956–1962.

Su, Z., Wang, J., Klein, P., Thompson, A. F., & Menemenlis, D. (2018). Ocean submesoscales as a key component of the global heat budget. *Nature Communications*, *9*(1), 1–8.

Whalen, C. B., de Lavergne, C., Garabato, A. C. N., Klymak, J. M., Mackinnon, J. A., & Sheen, K. L. (2020). Internal wave-driven mixing: governing processes and consequences for climate. *Nature Reviews Earth & Environment*, *1*(11), 606–621.

Zhao, Z., Alford, M. H., MacKinnon, J. A., & Pinkel, R. (2010). Long-range propagation of the semidiurnal internal tide from the Hawaiian Ridge. *Journal of Physical Oceanography*, *40*(4), 713–736.